

## RESEARCH ARTICLE

## TECHNIQUES AND RESOURCES

# Temporal ordering and registration of images in studies of developmental dynamics

Carmeline J. Dsilva<sup>1,\*</sup>, Bomyi Lim<sup>1,\*</sup>, Hang Lu<sup>2</sup>, Amit Singer<sup>3,4</sup>, Ioannis G. Kevrekidis<sup>1,4,‡</sup> and Stanislav Y. Shvartsman<sup>1,5,‡</sup>

## ABSTRACT

Progress of development is commonly reconstructed from imaging snapshots of chemical or mechanical processes in fixed tissues. As a first step in these reconstructions, snapshots must be spatially registered and ordered in time. Currently, image registration and ordering are often done manually, requiring a significant amount of expertise with a specific system. However, as the sizes of imaging data sets grow, these tasks become increasingly difficult, especially when the images are noisy and the developmental changes being examined are subtle. To address these challenges, we present an automated approach to simultaneously register and temporally order imaging data sets. The approach is based on vector diffusion maps, a manifold learning technique that does not require *a priori* knowledge of image features or a parametric model of the developmental dynamics. We illustrate this approach by registering and ordering data from imaging studies of pattern formation and morphogenesis in three model systems. We also provide software to aid in the application of our methodology to other experimental data sets.

**KEY WORDS:** Temporal ordering, Image registration, Vector diffusion maps, Zebrafish, *Drosophila*

## INTRODUCTION

In one of the common approaches to studies of developmental dynamics, a group of embryos is fixed and stained to visualize a particular biochemical or morphological process within a developing tissue. The developmental dynamics must then be reconstructed from multiple embryos, each of which contributes only a snapshot of the relevant process along its developmental trajectory (Jaeger et al., 2004; Fowlkes et al., 2008; Peter and Davidson, 2011). Importantly, the ‘age’ of any given embryo arrested in its development is often only approximately known. Typically, what is known is a certain time window to which a collection of embryos belongs (Castro et al., 2009; Ng et al., 2012; Richardson et al., 2014). Furthermore, images are often collected in different spatial orientations. In order to recover the developmental dynamics from such data sets, snapshots of different embryos must first be spatially aligned or registered, and then ordered in time.

Temporal ordering and registration of images can be done manually when the number of images is small and the differences between them are visually apparent. Fig. 1 shows a caricature of fish development that illustrates the processes of growth and patterning. In this case, temporal ordering can be accomplished by arranging the fish by size, which is monotonic with the developmental progress. Image registration is based on obvious morphological landmarks, such as the positions of the head and the fins. In contrast to this example, real data pose nontrivial challenges for both registration and temporal ordering. In general, the landmarks needed for registration, as well as the attributes that can be used to order the data, are not known *a priori*. Additional challenges arise from embryo-to-embryo variability, sample size and measurement noise.

We present a robust algorithmic approach to simultaneous registration and temporal ordering. In contrast to a number of previous methodologies (Greenspan et al., 1994; Rowley et al., 1998; Zhao et al., 2003; Zitová and Flusser, 2003; Hajnal and Hill, 2010; Dubuis et al., 2013), ours does not rely on the *a priori* knowledge of landmarks for registration or markers of developmental progression. The approach is based on vector diffusion maps (Singer and Wu, 2012), a manifold learning algorithm that simultaneously addresses the problems of registration and temporal ordering. This algorithm is one of several nonlinear dimensionality reduction techniques that have been developed over the past decade (Roweis and Saul, 2000; Tenenbaum et al., 2000; Belkin and Niyogi, 2003; Coifman et al., 2005; Coifman and Lafon, 2006) for applications ranging from the analysis of cryo-electron microscopy (cryo-EM) images of individual molecules (Singer et al., 2011; Zhao and Singer, 2014) to face recognition (Lafon et al., 2006) and the classification of CT scans (Fernández et al., 2014).

Here, the vector diffusion maps algorithm is adapted for the analysis of images of tissues in studies of developmental dynamics, with the main objective of revealing stereotypic developmental trajectories from fixed images. To illustrate our approach, we analyze four experimental data sets. The first two data sets come from live imaging studies of *Drosophila* and zebrafish embryogenesis. In both of these examples, the correct rotational orientation and temporal order are independently known, and these data sets will be used to validate our approach. Our third data set consists of images from fixed *Drosophila* embryos, for which the correct orientation and order are unknown; here, we will show how the algorithm can help uncover developmental dynamics that are not readily apparent. Our final data set consists of z-stacks of *Drosophila* wing discs, which we will use to illustrate how our methods can be used to analyze specific types of 3D imaging data. We also show how to compute an average trajectory from a set of registered and ordered fixed images to remove noise due to intersample variability and obtain a smooth description of the underlying developmental dynamics.

<sup>1</sup>Department of Chemical and Biological Engineering, Princeton University, Princeton, NJ 08544, USA. <sup>2</sup>School of Chemical and Biomolecular Engineering, Georgia Institute of Technology, Atlanta, GA 30332, USA. <sup>3</sup>Department of Mathematics, Princeton University, Princeton, NJ 08544, USA. <sup>4</sup>Program in Applied and Computational Mathematics, Princeton University, Princeton, NJ 08544, USA. <sup>5</sup>Lewis-Sigler Institute for Integrative Genomics, Princeton University, Princeton, NJ 08544, USA.

\*These authors contributed equally to this work

‡Authors for correspondence (yannis@princeton.edu; stas@princeton.edu)

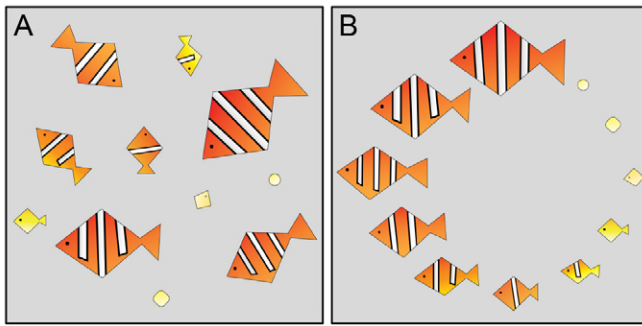


**Fig. 1. Caricature illustrating the tasks of image registration and temporal ordering.** (A) Images of 'samples', each in a different orientation and at a different stage of development. (B) Registered and ordered samples. For this caricature, the registration and ordering is straightforward because the data set is small, the landmarks are visually apparent, and the developmental changes are easy to recognize.

## RESULTS

### Vector diffusion maps for registration and temporal ordering

Vector diffusion maps (Singer and Wu, 2012) is a manifold learning technique developed for data sets that contain two sources of variability: geometric symmetries, such as rotations of the images, which one would like to factor out; and 'additional' directions of variability, such as temporal dynamics, which one would like to uncover. Vector diffusion maps combine two algorithms – angular synchronization (Singer, 2011) for image registration, and diffusion maps (Coifman et al., 2005) for extracting intrinsic low-dimensional structure in data – into a single computation. We will use the algorithm to register images of developing tissues with respect to planar rotations, as well as uncover the main direction of variability after removing rotational symmetries. Although, in general, images may contain variations due to rotations, translations and scaling, we will remove the relevant translations and/or scaling via relatively simple image preprocessing, and focus only on factoring out rotations using the vector diffusion maps algorithm. In the case that all relevant symmetries can be removed with straightforward preprocessing, our algorithms can extract the main direction of variability within the imaging data set. We assume that this main direction of remaining variability in these images is parametrized by the developmental time of each embryo. As a consequence, uncovering this direction should reveal the underlying dynamics.

Angular synchronization uses pairwise alignment information to register a set of images in a globally consistent way. A schematic illustration of angular synchronization is shown in Fig. 2A, where each image is represented as a vector, and the goal is to align the entire set of vectors given pairwise alignment measurements. We first compute the angles needed to align pairs of vectors (or images), which in general requires no notion of a template function (Ahuja et al., 2007; Sunday et al., 2013). In this work, we aligned pairs of images with respect to rotations by exhaustively searching over a discretized space of rotation angles to minimize the Euclidean distance between the pixels. However, pairwise alignments can also be computed by aligning appropriate image landmarks or features (Dryden and Mardia, 1998). When the data are noisy, these pairwise measurements may be inaccurate, and so we utilize all pairwise measurements to align the set of images robustly. Using the alignment angles between all pairs of vectors, angular synchronization finds the set of rotation angles (one angle for each vector) that is most

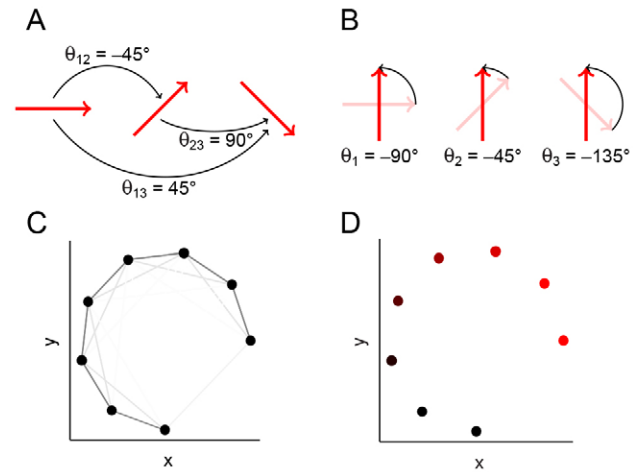


**Fig. 2. Schematic illustrating angular synchronization and diffusion maps.**

(A) A set of vectors, each in a different orientation. The pairwise alignment angles are indicated. (B) The vectors from A, each rotated about their midpoint so that the set is globally aligned. Note that the chosen rotation angles are consistent with the pairwise alignments in A: the difference between a pair of angles in B is the same as the pairwise angle in A. (C) Data points (black) that lie on a 1D nonlinear curve in two dimensions. Each pair of points is connected by an edge, and the edge weight is related to the Euclidean distance between the points through a Gaussian kernel (see algorithms in the supplementary material), so that pairs of data points that are close are connected by darker ('stronger') edges. (D) The data in C, colored by the first (non-trivial) eigenvector from the diffusion map computational procedure. The color intensity is monotonic with the perceived curve arc length, thus parametrizing the curve.

consistent with all pairwise measurements (see algorithms in the supplementary material); this is illustrated in Fig. 2B. In this schematic, registration via angular synchronization is trivial, as the pairwise measurements contain no noise. However, the algorithm can register data sets even when many of the pairwise measurements are inaccurate (Singer, 2011).

After removing variability due to rotations, the developmental dynamics may be revealed by ordering the data along the 1D curve that parametrizes most of the remaining variability in the data. Such a curve can be discovered using diffusion maps (Coifman et al., 2005), a nonlinear dimensionality reduction technique that reveals a parametrization of data that lies on a low-dimensional manifold in high-dimensional space. The idea is illustrated in Fig. 2C, where the data are 2D points that lie on a 1D (nonlinear) curve. We use local information about the data to find a parametrization that respects the underlying manifold geometry, so that points that are close in high-dimensional space (e.g. images which look similar) are close in our parametrization. This idea of locality is denoted by the weight of the edges in Fig. 2C: data points that are close are connected by dark edges and, clearly, the dark edges are more 'informative' about the low-dimensional structure of the data. The color in Fig. 2D depicts the 1D parametrization or ordering of the data that we can detect visually. A detailed example of using vector diffusion maps to register and order synthetic data is given in supplementary material Fig. S2, and a step-by-step tutorial of the diffusion maps implementation is provided with the software. In our working examples, each data point will be of much higher dimension (e.g. a pixelated image or 3D voxel data), and so we cannot extract this low-dimensional structure visually. Instead, we will use diffusion maps, which automatically uncovers a parametrization of our high-dimensional data from the eigenvectors of the appropriate matrix (see algorithms in the supplementary material). Furthermore, the

corresponding eigenvalues will allow us to test our assumption that our data approximately lie on a 1D manifold (see supplementary material Figs S3–S6).

### Method validation using live imaging

#### *Drosophila* gastrulation

To validate the proposed approach, we first applied our algorithm to a data set where the true temporal order and rotational orientation of the images were known *a priori*. This data set was obtained through live imaging near the posterior pole of a vertically oriented *Drosophila* embryo during the 20 min spanning the late stages of cellularization through early gastrulation. During this time window, the ventral furrow is formed where the ventral side buckles towards the center of the embryo, internalizing the future muscle cells and forming a characteristic ‘omega’ shape. Germband extension then causes cells from the ventral side to move towards the posterior pole of the embryo, and then wrap around to the dorsal side (Leptin, 2005). At the end of this process, cells that were originally on the ventral and posterior side of the embryo find themselves on the dorsal side, causing a similar omega to appear on the dorsal side.

Fig. 3A shows selected images from this live imaging data set, which contains 40 consecutive frames taken at 30 s intervals at a fixed position within a single embryo. Each image shows an optical cross-section near the posterior pole of a vertically oriented developing *Drosophila* embryo, with the nuclei labeled by Histone-RFP. Each frame was arbitrarily rotated, and the order of the frames was scrambled. The task is now to register these images and order them in time to reconstruct the developmental trajectory.

We used vector diffusion maps to register and order the images. Fig. 3B shows the images from Fig. 3A now registered and ordered; the real time for each frame is also indicated. With a small number of exceptions, the recovered ordering is consistent with the real-time dynamics. Fig. 3C,D show the correlations between the recovered and true angles and rank orders, respectively, for the entire data set.

Both the angles and the ranks are recovered with a high degree of accuracy. We note that determining which end of the trajectory corresponds to early in the developmental progression is a post-processing task that requires some *a priori* information.

To assess the robustness of the proposed methodology, we repeated this procedure with four additional data sets extracted from independent live imaging studies spanning the same developmental time period. The results are shown in Table 1. The errors in the recovered angles are all less than 10°, and the rank correlation coefficients are consistently greater than 95%, indicating that our methodology can reproducibly order data of this type.

#### Zebrafish epiboly

As another validation for the proposed methodology, we applied our algorithm to a time-lapse movie of zebrafish embryogenesis. We used publicly available live imaging data of zebrafish embryogenesis [https://zfin.org/zf\_info/movies/Zebrafish.mov (Karlstrom and Kane, 1996)]. Taken with a differential interference contrast (DIC) microscope, the movie records the first 17 h of zebrafish development, from the single-cell stage to 16-somite stage. We selected 120 consecutive frames from this movie that capture 5.5 h of epiboly (3.5–9 h after fertilization). In this experiment, embryos were immobilized for imaging so that the position and orientation remained fixed (Kane et al., 1996). At the start of the time window, cells have divided 10–11 times and have accumulated in a cell mass above the yolk. The cell mass is then compressed and the animal-vegetal axis of the embryo (vertical axis in Fig. 4) shortens to form a spherical embryo by the end of the fourth hour of development. Then, the yolk syncytial layer, which forms the boundary between the yolk and the cell mass, moves upward, forming a dome-shaped structure. During this stage, the cells rearrange to form a uniform layer about four cells thick. With time, this cell layer then spreads across the yolk and expands toward the vegetal pole. At the end of epiboly, the blastoderm completely engulfs the yolk.

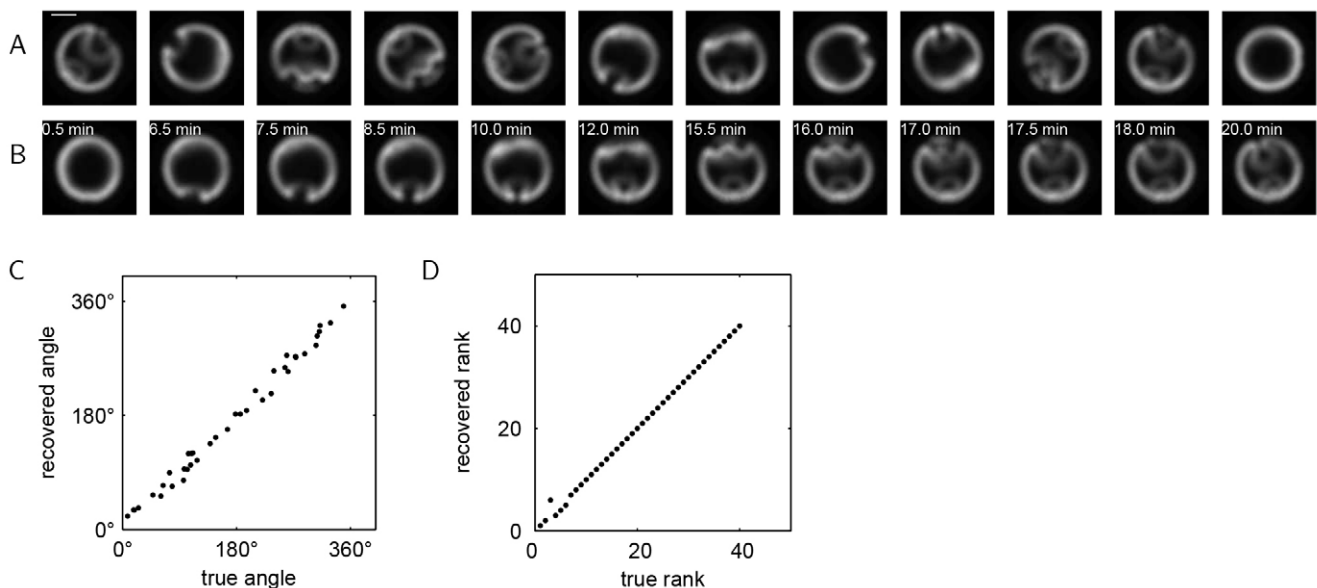


**Fig. 3. Method validation using live imaging of *Drosophila* embryos.** (A) Selected images from a live imaging study of a *Drosophila* embryo during gastrulation. Scale bar: 50  $\mu$ m. Each frame is in an arbitrary rotational orientation and the order of the frames has been shuffled. (B) Images from A registered and ordered by vector diffusion maps. The dorsal side of each embryo now appears at the top of each image and the ventral side appears at the bottom. The real time of each frame is also indicated, where  $t=0$  corresponds to the initiation of ventral furrow formation. (C) The correlation between the recovered rotation angle (using vector diffusion maps) and the true rotation angle. The average absolute error in the recovered angles is 8.37°. (D) The correlation between the recovered rank (using vector diffusion maps) and the true rank. The rank correlation coefficient is 0.9989 (see also Table 1).



**Table 1. Average error in the recovered angle and the rank correlation coefficient ( $\rho$ ) for five independent *Drosophila* live imaging studies**

| Movie index | Angle error (°) | $\rho$ |
|-------------|-----------------|--------|
| 1           | 8.37            | 0.9989 |
| 2           | 4.98            | 0.9994 |
| 3           | 6.47            | 0.9795 |
| 4           | 7.03            | 0.9953 |
| 5           | 3.04            | 0.9959 |

See also Fig. 3.

As in the example of *Drosophila* embryo live imaging, the 2D frames were randomly rotated and shuffled (Fig. 4A). We then used vector diffusion maps to register and order the frames. The results are shown in Fig. 4B. The recovered rotations and order are consistent with the expected developmental dynamics, as shown in the correlations between the recovered and true ranks (Fig. 4C). Quantitatively, the rank correlation coefficient for this data set is 0.9954, and the average error in the recovered angle is 4.14°. Some errors in ordering images of the early embryo result from slow cell movement during the early developmental stage when cells divide and accumulate above the yolk. During epiboly, cell movement is more dynamic and the recovered ordering is more consistent with the real dynamics.

In summary, we have shown that our approach to temporal ordering performs very well on imaging data of two different developmental processes (*Drosophila* gastrulation and zebrafish epiboly) taken with two different imaging methods (fluorescent microscopy and DIC), where the true temporal order is known *a priori*. Provided that significant dynamics exist within the data set and that the developmental trajectory is well sampled, the developmental dynamics can be recovered.

**Data sets with intersample variability**  
**Fixed images of *Drosophila* gastrulation**

We have analyzed how our algorithm performs on two model data sets where all images come from a single embryo. In practice, we are interested in cases in which each image comes from a different embryo, and the largest source of noise in the considered data set arises from embryo-to-embryo variability. To demonstrate that our methods are robust to such variations, we constructed a synthetic timecourse data set by selecting a random image from one of five *Drosophila* live imaging data sets (those data sets used in Fig. 3) at each time point. The resulting data set is spatially unregistered, scrambled in time, and reflects embryo-to-embryo variability. The median rank correlation coefficient when ordering such a synthetic timecourse using our methodology was 0.77, indicating that the algorithm can recover the temporal order even under noisy conditions.

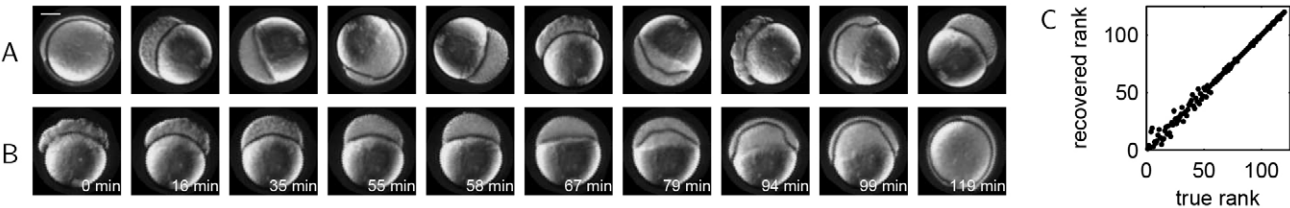
We then applied our approach to a data set where the true rotational orientation and temporal order were not known *a priori*.

Fig. 5A shows selected images from a set of 120 images of developing *Drosophila* embryos that cover a 30 min interval spanning late cellularization through gastrulation. This data set is more complex than the live imaging data sets in that it contains significantly more images, each of which provides information about tissue morphology and the spatial distribution of two regulatory proteins. Each image shows an optical cross-section of the posterior view of a different embryo at a different rotational orientation and fixed at a different (and unknown) developmental time. The nuclei (gray) were labeled with the DNA stain DAPI. Embryos were stained with an antibody that recognizes Twist (Twi, green), a transcription factor that specifies the cells of the future muscle tissue. Another signal is provided by the phosphorylated form of the extracellular signal regulated kinase [dpERK (ERK is also known as Rolled in *Drosophila*), red], an enzyme that, in this context, specifies a subset of neuronal cells (Lim et al., 2013).

Fig. 5B shows the selected images in Fig. 5A now registered and ordered using vector diffusion maps. Registered and ordered images of individual embryos can then be used to construct a representative average trajectory. Each snapshot in the average trajectory is the (weighted) average of a group of successive images from the registered and ordered data set (see smooth trajectories from registered and ordered images in the supplementary material). Averaging successive images removes some of the interembryo variability, so that sequential snapshots of this averaged trajectory, as shown in Fig. 5C, serve as a summary of the stereotypic developmental dynamics.

From this average trajectory, we can now easily see the developmental progression consistent with the known dynamics: dpERK first appears as two lateral peaks at the ventrolateral side of the embryo, and a third dpERK peak then appears at the dorsal side of the embryo. During mesoderm invagination, the two ventrolateral dpERK peaks merge together, eventually forming, together with Twi, the omega shape. The dorsal dpERK peak then disappears during germband extension as cells from the ventral side wrap around to the dorsal side. At the end of this process, similar omegas formed by Twi and dpERK appear on the dorsal side of the embryo; these patterns are most readily seen in the last image of Fig. 5C. Thus, vector diffusion maps can accomplish the tasks presented in the caricature in Fig. 1, even in the absence of information about image landmarks and without *a priori* knowledge of developmental features.

To evaluate the quality of our registration and ordering, we can use prior knowledge about the developmental system. The Twi signal is known to form a single peak at the ventralmost point of the embryo. We found that the standard deviation in the location of this peak in the set of registered images was ~8°, indicating that the algorithm successfully aligns the ventralmost points of the images. Because the developmental time of each embryo



**Fig. 4. Method validation using live imaging of a zebrafish embryo.** (A) Selected images from a movie of zebrafish epiboly. Scale bar: 200  $\mu$ m. Each frame is in an arbitrary rotational orientation and the order of the frames has been shuffled. (B) Images from A after registration and ordering using vector diffusion maps. The real time of each frame is also indicated. (C) Correlation between the rank recovered using vector diffusion maps and the true rank. The rank correlation coefficient is 0.9954. The larger errors in the recovered ranks towards the beginning of the trajectory are due to slow cell movement within that time window.

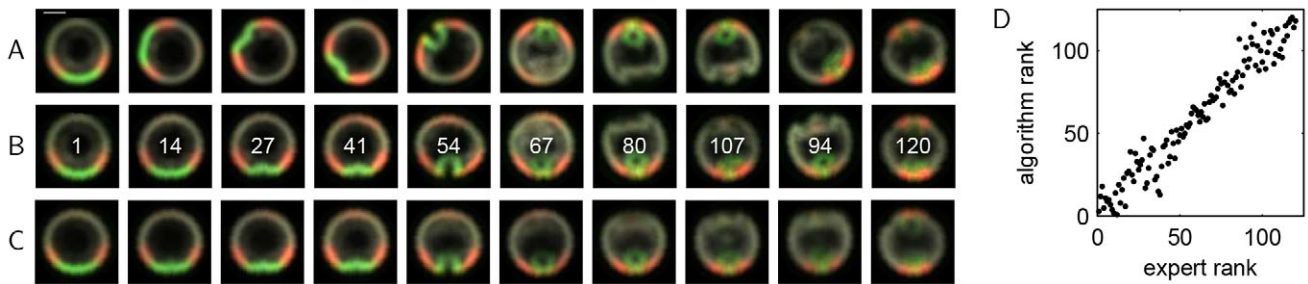


**Fig. 5. Analysis of images of fixed *Drosophila* embryos.** (A) Images of *Drosophila* embryos stained for nuclei (gray), Twi (green) and dpERK (red). Scale bar:  $\sim 50 \mu\text{m}$  (images have been rescaled to remove slight interembryo size variations). Each image is of a different embryo arrested at a different developmental time and in a different rotational orientation. (B) Data from A, registered and ordered using vector diffusion maps. The 'expert rank' for each image is indicated. (C) A representative developmental trajectory obtained from local averaging of the entire set of registered and ordered images (see smooth trajectories from registered and ordered images in the supplementary material). (D) Correlation between the image ranks calculated from the vector diffusion maps algorithm and the ranks obtained from ordering by an expert. The rank correlation coefficient is 0.9716.

cannot be easily estimated, we have few options for evaluating the quality of our temporal ordering. We compared the ordering obtained from vector diffusion maps with the ordering provided by a trained embryologist who is knowledgeable about the developmental progression and the important image features. The ranks from the ordering provided by the embryologist, which we will refer to as the 'expert rank', are indicated for the images in Fig. 5B, and the rank correlation (Fig. 5D) shows that our ordering is consistent with the expert ordering.

#### Fixed z-stacks of *Drosophila* wing discs

In this section we show that the approach can readily be applied to 3D data. We restrict ourselves to the case in which an obvious fixed axis exists, so that only rotations of the 3D data around this axis need be taken into account. This does not constitute an inherent limitation

for vector diffusion maps. Although, for simplicity, here we will not discuss the general case, incorporating general 3D symmetries is possible (Arie-Nachimson et al., 2012; Cucuringu et al., 2013; Wang and Singer, 2013).

To demonstrate this approach, we used an existing 3D data set of fixed *Drosophila* wing imaginal discs (Hamaratoglu et al., 2011). Imaginal discs are groups of progenitor cells in fly larva that will transform into specific organs during metamorphosis. The wing disc is an imaginal disc that gives rise to the wing, thorax and hinge. The data set is composed of 46 fixed wing discs with developmental times that range from 72 to 112 h after fertilization. Each disc contains 21 z-slices taken at  $1 \mu\text{m}$  intervals. The discs were dissected from larvae expressing the Dad-GFP reporter construct (green) and stained with antibodies that recognize Spalt (red), Wingless (gray) and Patched (gray), the

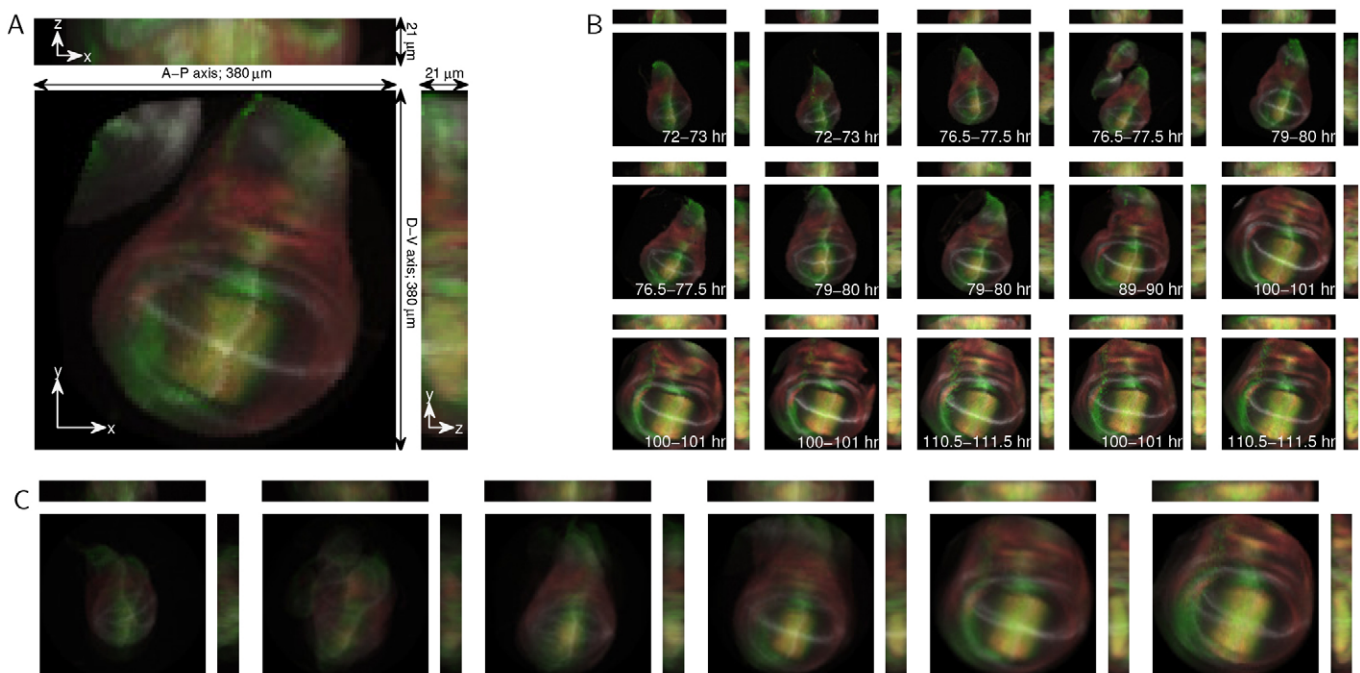


**Fig. 6. Analysis of 3D *Drosophila* wing disc z-stacks.** (A) Maximum projections of an example 3D *Drosophila* wing disc z-stack. The anterior-posterior (A-P) and dorsal-ventral (D-V) axes are indicated. Discs express the Dad-GFP reporter construct (green) and are stained for Spalt (red), Wingless (gray) and Patched (gray). Projections along the x, y and z axes are shown. (B) Example 3D images, ordered using diffusion maps. The time cohort, as assessed by an expert, is indicated for each image, and the rank correlation coefficient between the diffusion maps ordering and the expert timing is 0.9427. (C) The average developmental trajectory for the registered and ordered images.

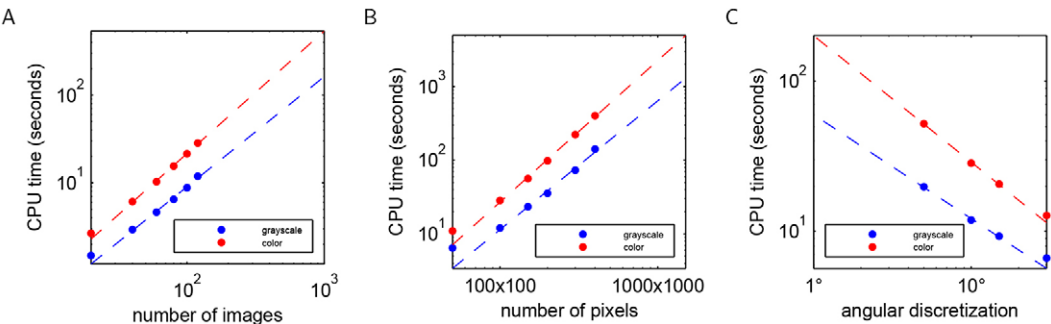


**Fig. 7. Computational requirements for the presented methodology.** (A) CPU time as a function of the number of images in the data set (for 100×100 pixel images and 10° angular discretization). Empirically, the CPU time scales as  $\sim n^{1.33}$  in number of images. (B) CPU time as a function of the number of pixels in the images (for 120 images and 10° angular discretization). Empirically, the CPU time scales as  $\sim n^{1.83}$  in the number of pixels. (C) CPU time as a function of the number of rotations (for 120 images of 100×100 pixels). Empirically, the CPU time scales as  $\sim n^{-0.77}$  in the angular discretization.

factors that play important roles in disc patterning and growth (Fig. 6A).

In the wing disc, the anterior-posterior and dorsal-ventral axes are significantly longer than the third principal axis (see Fig. 6A). Therefore, we need not consider registration in all three dimensions, and can instead focus on registering the wing discs with respect to rotations only in the *x-y* plane. To register the data, we first aligned the maximum intensity projections using angular synchronization. We then used these rotations to register the full 3D data in the *x-y* plane. Because the maximum intensity projections are 2D images, this step is no more computationally intensive than in the previous examples. Such an approach is possible when there are distinct major and minor axes within a 3D sample, which reduces the rotational degrees of freedom.

We then used diffusion maps to order the registered 3D data. Fig. 6B shows selected images from the data set ordered by diffusion maps. In the original data set, each disc was assigned to one of six time classes (72-73, 76.5-77.5, 79-80, 89-90, 100-101 and 110.5-111.5 h after fertilization, Fig. 6B) by an expert. In the ordered set, the size of the wing disc grows, and the intensity of the Dad-GFP signal increases as a function of time. The rank correlation coefficient based on the time class is 0.9436. The registration errors are primarily due to some wing discs having extra tissue attached to them (such as the image in Fig. 6A and the fourth image in Fig. 6B). Even with such obstructions, we can accurately order the images and extract a stereotypical developmental trajectory, as shown in Fig. 6C, by averaging (see smooth trajectories from registered and ordered images in the supplementary material). We can now clearly see the growth of the wing disc, even though averaging somewhat blurs some finer scale structures.

Computational requirements

The computational costs for our methodology are outlined in Fig. 7 and Table 2. The computational time is a function of the number of images in the data set, the number of pixels in each point, and the angular resolution to compute the pairwise rotations (see

registering images in the supplementary material). Furthermore, the computation of the pairwise rotational alignments, which accounts for the majority of the computational time, can be easily parallelized, and only a subsample of the pairwise alignments need be computed for larger data sets for accurate recovery of the underlying rotations (Singer, 2011). Because the computational cost increases with the image resolution, we chose to subsample all of our data sets to 100×100 pixels. This resolution allowed us to rapidly analyze our data sets while retaining all of the relevant developmental features. However, as can be seen from the computational costs in Fig. 7 and Table 2, it is feasible to use our algorithms to analyze higher-resolution images.

The requisite user intervention and parameter tuning required for our method is relatively minor. As a first step, images must be preprocessed so that the Euclidean distance between the pixels is informative. Our software provides several preprocessing options (such as blurring, rescaling and mean-centering), as well as some guidance for what options to select depending on the system of interest. Two algorithmic parameters – the angular discretization to compute the pairwise alignments, and the diffusion maps kernel scale that determines which data points are ‘close’ (see Fig. 2 and algorithms in the supplementary material) – must also be defined. We also provide some guidance on selecting these parameters, and we find that the results are robust to both of these parameters. Overall, the tasks of image preprocessing and parameter selection are relatively simple compared with the manual registration and ordering of images, and so this methodology is promising for much larger imaging data sets that are impractical to evaluate manually.

DISCUSSION

Temporal ordering of large-scale data has been performed in the context of molecular profiling studies, in which data points are vectors describing the expression levels of different mRNAs (Gupta and Bar-Joseph, 2008; Anavy et al., 2014; Trapnell et al., 2014). At the same time, temporal ordering of imaging data sets was undertaken with a significant amount of manual intervention and

**Table 2. The algorithm settings and computational requirements for the data sets analyzed in Figs 3-6**

| Data set                               | Data type | Number of channels | Number of images | Number of pixels | Angular discretization (°) | CPU time (s) |
|--|-----------|--------------------|------------------|------------------|----------------------------|--------------|
| <i>Drosophila</i> gastrulation (live)  | 2D        | 1                  | 40               | 100×100          | 10                         | 3.2          |
| Zebrafish epiboly                      | 2D        | 1                  | 120              | 100×100          | 10                         | 13           |
| <i>Drosophila</i> gastrulation (fixed) | 2D        | 3                  | 120              | 100×100          | 10                         | 29           |
| <i>Drosophila</i> wing discs           | 3D        | 3                  | 46               | 100×100×21       | 10                         | 12           |

All times are reported for an Intel Core i7 2.93 GHz processor.



using registered images as a starting point (Fowlkes et al., 2008; Surkova et al., 2008; Yuan et al., 2014), or using some *a priori* knowledge of the developmental processes under examination (Dubuis et al., 2013). In contrast to most of the existing registration approaches, which rely on a knowledge of appropriate landmarks in the images (Dryden and Mardia, 1998), such as the eyes in face-recognition applications (Zhao et al., 2003), algorithms based on angular synchronization can register images even in the absence of such information, making them relevant for a wide variety of applications.

Angular synchronization and vector diffusion maps have been used to reconstruct molecular shapes from cryo-electron microscopy images (Singer et al., 2011; Singer and Wu, 2012; Zhao and Singer, 2014). Because of high levels of instrument noise in these data, thousands of images were needed for successful shape reconstruction. Based on the results presented here, we expect that much smaller data sets will be sufficient for successful reconstruction of developmental trajectories from snapshots of fixed tissues. In general, the size of the data set required for accurate registration and ordering is a function of the instrument noise, interembryo variability, and the complexity of the developmental dynamics.

The benefits of our approach to image data mining are twofold. First, the algorithm can accomplish the tasks of registration and ordering in a single step. Furthermore, because our methodology is nonlinear, it can successfully order data sets that contain complex dynamics (see supplementary material Table S1 for a comparison of ordering using linear principal component analysis versus vector diffusion maps for the data sets presented in this paper). We expect nonlinear techniques to be necessary for larger data sets that span a wider dynamic range. The main utility of our proposed methodology lies in the analysis of data sets containing hundreds of images from systems that have not been well studied. For such data sets, manual ordering of the images can be nontrivial, and our algorithms can clearly accelerate uncovering of the underlying developmental dynamics.

We acknowledge that our methods, although general, do have limitations. The first is that we require enough data to sufficiently sample the developmental trajectory. Therefore, for very small and/or very noisy data sets, our algorithms might fail. Second, the pertinent image features need to be large compared with the noise and the image resolution. In all of our examples, the relevant expression patterns and morphological structures span several pixels and are large compared with both the instrument noise and embryo-to-embryo variability, making the Euclidean distance between pixels a good measure of image similarity.

Vector diffusion maps allow us to automatically register images, which is an essential task for many applications. Simultaneously, the algorithm provides us with parameters to describe each image. In the examples presented here, we have focused on ordering the images in time using the first vector diffusion maps coordinate. In general, we can recover several coordinates that concisely and comprehensively describe the data set. This parametrization can then be used for typical data analysis tasks, such as outlier detection and model fitting. Furthermore, images taken from different viewing directions can be analyzed, as the vector diffusion maps parametrization will organize the images according to the viewing angle (Singer et al., 2011). Another direction for future work is related to the joint analysis of data sets provided by different imaging approaches, such as merging live imaging data of tissue morphogenesis with snapshots of cell signaling and gene expression from fixed embryos (Rübel et al., 2010; Krzic et al., 2012; Dsilva

et al., 2013; Ichikawa et al., 2014). It would also be interesting to explore the connections between our proposed approach and recently developed methods for the ordering and classification of face images (Kemelmacher-Shlizerman et al., 2011, 2014). Given the rapidly increasing volumes of imaging data from studies of multiple developmental systems, we expect that the dimensionality reduction approaches discussed in this work will prove increasingly useful for biologists and motivate future applications and algorithmic advances.

## MATERIALS AND METHODS

### *Drosophila* embryo experiments

Oregon-R was used as the wild-type *Drosophila* strain. Embryos were collected and fixed at 22°C. Monoclonal rabbit anti-dpERK (1:100, Cell Signaling, cat. 4370) and rat anti-Twist (1:500; a gift from Eric Wieschaus, Princeton University) were used to stain proteins of interest; DAPI (1:10,000, Vector Laboratories) was used to visualize nuclei, and Alexa Fluor secondary antibodies (1:500, Invitrogen) were used. The Histone-RFP strain (Bloomington Stock Center) was used to obtain time-lapse movies of gastrulating embryos at 22°C. Live embryos were loaded to the microfluidic device with PBST (PBS with 0.02% Triton X-100) to keep them oxidized, and fixed embryos were loaded with 90% glycerol.

### *Drosophila* embryo microscopy

A Nikon A1-RS scanning confocal microscope and Nikon 60× Plan-Apo oil objective were used to image *Drosophila* embryos. Embryos were collected, stained, and imaged together under the same microscope settings. End-on imaging was performed using the microfluidics device described previously (Chung et al., 2011). Images were collected at the focal plane ~90 μm from the posterior pole of the embryo (see supplementary material Fig. S1).

### Image preprocessing

Images were subsampled, normalized, blurred and centered prior to diffusion maps analysis to remove any variations due to the experimental and imaging framework. Details of the specific preprocessing operations applied to each imaging data set are given in the image preprocessing section in the supplementary material.

### Software and imaging data

All algorithms and analysis were implemented in MATLAB (R2013b, MathWorks) and are described further in the methods in the supplementary material. Software, including documentation and tutorials, along with the full imaging data sets used in this paper are available at [genomics.princeton.edu/stas/publications.html](http://genomics.princeton.edu/stas/publications.html) under ‘Code for the temporal ordering and registration of images in studies of developmental dynamics’.

### Acknowledgements

We thank Fisun Hamaratoglu and Markus Affolter for providing the wing disc data; and Angela DePace, Granton Jindal, Adam Finkelstein, Thomas Funkhouser and John Storey for helpful discussions.

### Competing interests

The authors declare no competing or financial interests.

### Author contributions

Scientific approaches were developed by C.J.D., B.L., H.L., A.S., I.G.K. and S.Y.S. Experiments were performed by B.L. Data analysis was performed by C.J.D. and B.L. The manuscript was prepared and edited by C.J.D., B.L., H.L., A.S., I.G.K. and S.Y.S.

### Funding

C.J.D. was supported by the Department of Energy Computational Science Graduate Fellowship (CSGF) [DE-FG02-97ER25308] and the National Science Foundation Graduate Research Fellowship [DGE 1148900]. B.L. and S.Y.S. were supported by the National Institutes of Health [R01GM086537]. H.L. was supported by the National Science Foundation Grant Emerging Frontiers in Research and Innovation (EFRI) [1136913]. A.S. was supported by the Air Force

Office of Scientific Research [FA9550-12-1-0317]. I.G.K. was supported by the National Science Foundation (CS&E Program). Deposited in PMC for release after 12 months.

#### Supplementary material

Supplementary material available online at <http://dev.biologists.org/lookup/suppl/doi:10.1242/dev.119396/-/DC1>

#### References

- Ahuja, S., Kevrekidis, I. G. and Rowley, C. W. (2007). Template-based stabilization of relative equilibria in systems with continuous symmetry. *J. Nonlinear Sci.* **17**, 109-143.
- Anavy, L., Levin, M., Khair, S., Nakanishi, N., Fernandez-Valverde, S. L., Degnan, B. M. and Yanai, I. (2014). BLIND ordering of large-scale transcriptomic developmental timecourses. *Development* **141**, 1161-1166.
- Arie-Nachimson, M., Kovalsky, S. Z., Kemelmacher-Shlizerman, I., Singer, A. and Basri, R. (2012). Global motion estimation from point matches. In *Second International Conference on 3D Imaging, Modeling, Processing, Visualization and Transmission (3DIMPVT) 2012*, pp. 81-88. IEEE.
- Belkin, M. and Niyogi, P. (2003). Laplacian eigenmaps for dimensionality reduction and data representation. *Neural Comput.* **15**, 1373-1396.
- Castro, C., Luengo-Oroz, M. A., Desnoullez, S., Duloquin, L., Fernandez-de-Manuel, L., Montagna, S., Ledesma-Carbayo, M. J., Bourguine, P., Peyrieras, N. and Santos, A. (2009). An automatic quantification and registration strategy to create a gene expression atlas of zebrafish embryogenesis. *Conf. Proc. IEEE Eng. Med. Biol. Soc.* **2009**, 1469-1472.
- Chung, K., Kim, Y., Kanodia, J. S., Gong, E., Shvartsman, S. Y. and Lu, H. (2011). A microfluidic array for large-scale ordering and orientation of embryos. *Nat. Methods* **8**, 171-176.
- Coifman, R. R. and Lafon, S. (2006). Geometric harmonics: a novel tool for multiscale out-of-sample extension of empirical functions. *Appl. Comput. Harmon. Anal.* **21**, 31-52.
- Coifman, R. R., Lafon, S., Lee, A. B., Maggioni, M., Nadler, B., Warner, F. and Zucker, S. W. (2005). Geometric diffusions as a tool for harmonic analysis and structure definition of data: Diffusion maps. *Proc. Natl. Acad. Sci. USA* **102**, 7426-7431.
- Cucuringu, M., Singer, A. and Cowburn, D. (2013). Eigenvector synchronization, graph rigidity and the molecule problem. *Inf. Inference* **1**, 21-67.
- Dryden, I. L. and Mardia, K. V. (1998). *Statistical Shape Analysis*. John Wiley.
- Dsilva, C. J., Talmon, R., Rabin, N., Coifman, R. R. and Kevrekidis, I. G. (2013). Nonlinear intrinsic variables and state reconstruction in multiscale simulations. *J. Chem. Phys.* **139**, 184109.
- Dubuis, J. O., Samanta, R. and Gregor, T. (2013). Accurate measurements of dynamics and reproducibility in small genetic networks. *Mol. Syst. Biol.* **9**, 639.
- Fernández, Á., Rabin, N., Coifman, R. R. and Eckstein, J. (2014). Diffusion methods for aligning medical datasets: location prediction in CT scan images. *Med. Image Anal.* **18**, 425-432.
- Fowlkes, C. C., Hendriks, C. L., Keränen, S. V. E., Weber, G. H., Rübél, O., Huang, M.-Y., Chatoor, S., DePace, A. H., Simirenko, L., Henriquez, C. et al. (2008). A quantitative spatiotemporal atlas of gene expression in the drosophila blastoderm. *Cell* **133**, 364-374.
- Greenspan, H., Belongie, S., Goodman, R. and Perona, P. (1994). Rotation invariant texture recognition using a steerable pyramid. In *Proceedings of the 12th IAPR International Conference on Pattern Recognition*, Vol. 2, pp. 162-167.
- Gupta, A. and Bar-Joseph, Z. (2008). Extracting dynamics from static cancer expression data. *IEEE/ACM Trans. Comput. Biol. Bioinform.* **5**, 172-182.
- Hajnal, J. V. and Hill, D. L. (2010). *Medical Image Registration*. CRC Press.
- Hamaratoglu, F., de Lachapelle, A. M., Pyrowolakis, G., Bergmann, S. and Affolter, M. (2011). Dpp signaling activity requires Pentagone to scale with tissue size in the growing Drosophila wing imaginal disc. *PLoS Biol.* **9**, e1001182.
- Ichikawa, T., Nakazato, K., Keller, P. J., Kajiura-Kobayashi, H., Stelzer, E. H. K., Mochizuki, A. and Nonaka, S. (2014). Live imaging and quantitative analysis of gastrulation in mouse embryos using light-sheet microscopy and 3D tracking tools. *Nat. Protoc.* **9**, 575-585.
- Jaeger, J., Surkova, S., Blagov, M., Janssens, H., Kosman, D., Kozlov, K. N., Manu, Myasnikova, E., Vanario-Alonso, C. E., Samsonova, M. et al. (2004). Dynamic control of positional information in the early Drosophila embryo. *Nature* **430**, 368-371.
- Kane, D. A., Hammerschmidt, M., Mullins, M. C., Maischein, H.-M., Brand, M., van Eeden, F., Furutani-Seiki, M., Granato, M., Haffter, P., Heisenberg, C.-P. et al. (1996). The zebrafish epiboly mutants. *Development* **123**, 47-55.
- Karlstrom, R. O. and Kane, D. A. (1996). A flipbook of zebrafish embryogenesis. *Development* **123**, 461-462.
- Kemelmacher-Shlizerman, I., Shechtman, E., Garg, R. and Seitz, S. M. (2011). Exploring photobios. *ACM Trans. Graph.* **30**, 61.
- Kemelmacher-Shlizerman, I., Suwajanakorn, S. and Seitz, S. M. (2014). Illumination-aware age progression. In *IEEE Conference on Computer Vision and Pattern Recognition (CVPR) 2014*, pp. 3334-3341.
- Krzic, U., Gunther, S., Saunders, T. E., Streichan, S. J. and Hufnagel, L. (2012). Multiview light-sheet microscope for rapid in toto imaging. *Nat. Methods* **9**, 730-733.
- Lafon, S., Keller, Y. and Coifman, R. R. (2006). Data fusion and multicue data matching by diffusion maps. *IEEE Trans. Pattern Anal. Mach. Intell.* **28**, 1784-1797.
- Leptin, M. (2005). Gastrulation movements: the logic and the nuts and bolts. *Dev. Cell* **8**, 305-320.
- Lim, B., Samper, N., Lu, H., Rushlow, C., Jiménez, G. and Shvartsman, S. Y. (2013). Kinetics of gene derepression by ERK signaling. *Proc. Natl. Acad. Sci. USA* **110**, 10330-10335.
- Ng, L. L., Sunkin, S. M., Feng, D., Lau, C., Dang, C. and Hawrylycz, M. J. (2012). Large-scale neuroinformatics for in situ hybridization data in the mouse brain. *Int. Rev. Neurobiol.* **104**, 159-182.
- Peter, I. S. and Davidson, E. H. (2011). A gene regulatory network controlling the embryonic specification of endoderm. *Nature* **474**, 635-639.
- Richardson, L., Stevenson, P., Venkataraman, S., Yang, Y., Burton, N., Rao, J., Christiansen, J. H., Baldock, R. A. and Davidson, D. R. (2014). EMAGE: electronic mouse atlas of gene expression. In *Mouse Molecular Embryology* (ed. M. Lewandoski), pp. 61-79. Springer.
- Roweis, S. T. and Saul, L. K. (2000). Nonlinear dimensionality reduction by locally linear embedding. *Science* **290**, 2323-2326.
- Rowley, H. A., Baluja, S. and Kanade, T. (1998). Rotation invariant neural network-based face detection. In *IEEE Computer Society Conference on Computer Vision and Pattern Recognition 1998*, pp. 38-44.
- Rübél, O., Ahern, S., Bethel, E. W., Biggin, M. D., Childs, H., Cormier-Michel, E., DePace, A., Eisen, M. B., Fowlkes, C. C., Geddes, C. G. R. et al. (2010). Coupling visualization and data analysis for knowledge discovery from multi-dimensional scientific data. *Procedia Comput. Sci.* **1**, 1757-1764.
- Singer, A. (2011). Angular synchronization by eigenvectors and semidefinite programming. *Appl. Comput. Harmon. Anal.* **30**, 20-36.
- Singer, A. and Wu, H.-T. (2012). Vector diffusion maps and the connection Laplacian. *Commun. Pure Appl. Math.* **65**, 1067-1144.
- Singer, A., Zhao, Z., Shkolnisky, Y. and Hadani, R. (2011). Viewing angle classification of cryo-electron microscopy images using eigenvectors. *SIAM J. Imaging Sci.* **4**, 723-759.
- Sonday, B., Singer, A. and Kevrekidis, I. G. (2013). Noisy dynamic simulations in the presence of symmetry: data alignment and model reduction. *Comput. Math. Appl.* **65**, 1535-1557.
- Surkova, S., Kosman, D., Kozlov, K., Manu, Myasnikova, E., Samsonova, A. A., Spirov, A., Vanario-Alonso, C. E., Samsonova, M. and Reinitz, J. (2008). Characterization of the Drosophila segment determination morphome. *Dev. Biol.* **313**, 844-862.
- Tenenbaum, J. B., De Silva, V. and Langford, J. C. (2000). A global geometric framework for nonlinear dimensionality reduction. *Science* **290**, 2319-2323.
- Trapnell, C., Cacchiarelli, D., Grimsby, J., Pokharel, P., Li, S., Morse, M., Lennon, N. J., Livak, K. J., Mikkelsen, T. S. and Rinn, J. L. (2014). The dynamics and regulators of cell fate decisions are revealed by pseudotemporal ordering of single cells. *Nat. Biotechnol.* **32**, 381-386.
- Wang, L. and Singer, A. (2013). Exact and stable recovery of rotations for robust synchronization. *Info. Inference* **2**, 145-193.
- Yuan, L., Pan, C., Ji, S., McCutchan, M., Zhou, Z.-H., Newfeld, S. J., Kumar, S. and Ye, J. (2014). Automated annotation of developmental stages of Drosophila embryos in images containing spatial patterns of expression. *Bioinformatics* **30**, 266-273.
- Zhao, Z. and Singer, A. (2014). Rotationally invariant image representation for viewing direction classification in cryo-EM. *J. Struct. Biol.* **186**, 153-166.
- Zhao, W., Chellappa, R., Phillips, P. J. and Rosenfeld, A. (2003). Face recognition: a literature survey. *ACM Comput. Surveys (CSUR)* **35**, 399-458.
- Zitová, B. and Flusser, J. (2003). Image registration methods: a survey. *Image Vis. Comput.* **21**, 977-1000.



# Supplemental Information

## Materials and Methods

### Image preprocessing

Before applying vector diffusion maps, images must be preprocessed so that the Euclidean distance between the image pixels is informative: we need images who are developmentally similar to have relatively small Euclidean distances, and images who are at disparate developmental time points to have relatively large distances. We must preprocess images to remove any experimental and imaging artifacts, so that most of the variation is relevant to the developmental dynamics.

The relevant image operations are listed below for our general purposes, along with the relevant MATLAB functions.

**Intensity normalization** Contrast-limited adaptive histogram equalization (using the `adapthisteq` function with an  $8 \times 8$  tile grid, and a uniform distribution for the intensities with a clip limit of 0.01) is used to normalize the intensities of signals whose absolute intensity is not meaningful/informative.

**Blur** The `imfilter` function with a disc filter is used to blur signals whose small-scale structure is not informative.

**Intensity scaling (multichannel images only)** The `immultiply` function is used to scale signal intensities. This is important for multichannel images, as it determines the (relative) contributions of the various signals.

**Mean-centering** The Canny method (Canny, 1986) is used to detect the edges of the object in each image (using the `edge` function). The image is then translated so that the object (as determined by extremities of the detected edges) is centered.

**Size scaling** For images whose relative size is unimportant to the developmental dynamics, the images are rescaled/dilated so that the object size (as determined by extremities of the detected edges) is constant (we set this to be 80% of the total image).

**Removing corners** The image is cropped/filtered using a disc centered in the middle of the image and whose diameter is equal to the number of pixels; any pixels outside of this disc are set to 0 (no intensity). This removes any corner effects under rotations.

### *Drosophila* gastrulation (live)

The original image resolution is  $512 \times 512$  for the live *Drosophila* embryo images. All images were subsampled to  $100 \times 100$  pixels for analysis, as this was found to be a sufficient resolution to retain all of the major developmental features within the data set. Images were normalized, and then blurred with a filter of radius 5% of the total image (5 pixels). Images were not mean-centered or rescaled, as the entire live imaging data set was approximately centered already.

### Zebrafish epiboly

The original image resolution was  $320 \times 288$  for the zebrafish images. A 16-pixel border was removed from the left and right sides to make the images square, and all images were then subsampled to  $100 \times 100$  pixels for analysis, as this was found to be a sufficient resolution to retain all of the major developmental features within the data set. Images were not normalized or blurred. Images were mean-centered so that the embryo in each frame was (approximately) centered. Images were not rescaled for size, as changes in overall size are important.

### *Drosophila* gastrulation (fixed)

The original image resolution was  $1024 \times 1024$  for the fixed *Drosophila* images. All images were subsampled to  $100 \times 100$  pixels for analysis, as this was found to be a sufficient resolution to retain all of the major developmental features within the data set. The nuclei channel was normalized, and all channels were blurred with a filter of radius 5% of the total image (5 pixels) to remove the effects of individual nuclei. The nuclei channel was scaled by half; because this signal occupies a larger fraction of the image relative to the other signals, its overall contribution is large, and so we downscaled it so that each signal would have more comparable weight in the algorithm. The images were mean-centered and scaled to have a constant size using the nuclei signal to detect the edges of the embryo within the frame.

### *Drosophila* wing discs

The original image resolution was  $1024 \times 1024$  for the wing disc z-stacks. Each of the original wing disc z-stacks contains 30–40 images. All images were subsampled to  $100 \times 100$  pixels for analysis, as this was found to be a sufficient resolution to retain all of the major developmental

features within the data set. Each wing disc z-stack was reduced to a 21-image stack, consisting of the brightest image and the 10 images above and below. No channels were normalized or blurred in the images, and the channel intensities were kept at their imaging values. Images were mean-centered using the Wingless/Patched signal to detect the edges of the sample. Images were not rescaled for size, as changes in overall size are important.

## Algorithms

We demonstrate the algorithms for registration and temporal ordering using a synthetic data set. The relatively simple dynamics of this data set allows us to easily visualize and illustrate the main features of the different algorithms. Motivated by the geometry of our *Drosophila* embryo images, we construct a sequence of concentration profiles defined on a ring, and rotate each ring randomly around its center; an example is shown in Fig. S2A. Rotation of the ring corresponds to shifting (with periodic boundary conditions) the one-dimensional concentration profile shown at the bottom of Fig. S2A (the symmetry group is  $SO(2)$ , the group of all two-dimensional proper rotations). Each concentration profile is a noisy Gaussian (shown in Fig. S2B), and the Gaussians increase in intensity as a function of “time”. We discretize the profiles into 100 points, so our numerical data will be 100-dimensional vectors (the corresponding symmetry group for the discretized profiles is  $\mathbb{Z}_{100}$ , the group of integers modulo 100). Fig. S2C shows the entire data set; the concentration profiles have been stacked in an array, so that each row corresponds to a single profile. Because the profiles are unregistered and unordered, the underlying dynamics (a Gaussian whose amplitude grows in time) are not readily apparent.

### Angular synchronization (Singer, 2011)

Let  $x_1, \dots, x_m$  denote the signals that we wish to align with respect to rotations; each signal is a function defined on the unit circle (on the plane). First assume that each signal  $x_i$  is a *noisy* rotated copy of the underlying signal  $x_{true}$  (which we are *not* given), such that

$$x_i = f(x_{true}, \theta_i) + \xi_i \quad (1)$$

where the function  $f(x_{true}, \theta_i)$  rotates the signal  $x_{true}$  by  $\theta_i$  degrees, and  $\xi_i$  is a (typically Gaussian) noise term. Our goal is to recover  $\theta_1, \dots, \theta_m$ . Up to noise,

$$x_i \approx f(x_j, \theta_i - \theta_j); \quad (2)$$

note that (2) does not require knowledge of  $x_{true}$ . We can obtain an *estimate* of  $\theta_i - \theta_j$  by computing the rotation that optimally aligns  $x_j$  to  $x_i$ , i.e.,

$$\theta_i - \theta_j \approx \theta_{ij} = \arg \min_{\theta} \|x_i - f(x_j, \theta)\|^2. \quad (3)$$

Practically, the signals are discretized in a  $n$ -long vector (the local intensity at  $n$  equidistant points around the circle); rotating the function by an angle  $\theta$  then corresponds to cyclically shifting the elements of  $x_i$  by  $\frac{\theta_i}{2\pi}n$  (rounded to the nearest integer to obtain a valid shift). For the one-dimensional discretized profiles shown in Fig. S2, we exhaustively search over all  $n = 100$  possible shifts of the signals to obtain the optimal angles in (3). Alternatively, for continuous signals, an optimization algorithm can be used (Ahuja et al., 2007).

Rather than work with the angles  $\theta_{ij}$  directly, it is more convenient to consider the rotation matrices,

$$R(\theta_{ij}) = \begin{bmatrix} \cos(\theta_{ij}) & -\sin(\theta_{ij}) \\ \sin(\theta_{ij}) & \cos(\theta_{ij}) \end{bmatrix}, \quad (4)$$

which we can think of as operating on the points of the unit circle (on the plane) on which our signal is defined. Successive rotations correspond to multiplication of the corresponding rotation matrices:  $R(\alpha_1 + \alpha_2) = R(\alpha_1)R(\alpha_2)$ . Due to the orthogonality of rotation matrices,  $R(-\alpha) = R(\alpha)^T$ .

Let  $d$  denote the dimension of the rotation matrices we are considering (for planar rotations,  $R(\theta_{ij}) \in \mathbb{R}^{2 \times 2}$  and  $d = 2$ ). We construct the matrix  $H \in \mathbb{R}^{md \times md}$ , where  $H$  is an  $m \times m$  matrix of  $d \times d$  blocks, with the  $i, j^{th}$  block of  $H$ ,  $H_{ij}$ , defined as

$$H_{ij} = R(\theta_{ij}). \quad (5)$$

Under our assumption that  $\theta_{ij} \approx \theta_i - \theta_j$ ,  $H_{ij} \approx R(\theta_i)R(\theta_j)^T$  and

$$H \approx \begin{bmatrix} R(\theta_1) \\ R(\theta_2) \\ \vdots \\ R(\theta_m) \end{bmatrix} [R(\theta_1)^T R(\theta_2)^T \dots R(\theta_m)^T]. \quad (6)$$

It follows directly from (6) that the top block eigenvector of  $H$  contains our best estimates of  $R(\theta_1), R(\theta_2), \dots, R(\theta_m)$ . Let  $\phi_1, \phi_2, \dots, \phi_{md}$  denote the eigenvectors of  $H$  ordered so that  $|\lambda_1| \geq |\lambda_2| \geq \dots \geq |\lambda_{md}|$ , where  $\lambda_i$  is the eigenvalue corresponding to  $\phi_i$ . Then,

$$\hat{R} = \begin{bmatrix} \hat{R}_1 \\ \hat{R}_2 \\ \vdots \\ \hat{R}_m \end{bmatrix} = \begin{bmatrix} | & | & \dots & | \\ \phi_1 & \phi_2 & \dots & \phi_d \\ | & | & \dots & | \end{bmatrix}, \quad (7)$$

where  $\hat{R}_i \in \mathbb{R}^{d \times d}$  is (nearly) the estimate for  $R(\theta_i)$ . To obtain our estimate of  $R(\theta_i)$ , denoted  $R_{i,est}$ , we project  $\hat{R}_i$  onto the closest orthogonal matrix,

$$R_{i,est} = U_i V_i^T, \quad (8)$$

where  $U_i$  and  $V_i$  are the left and right singular vectors, respectively, of  $\hat{R}_i$ . We adjust the sign of  $\phi_1$  so that  $\det(R_{i,est}) = +1$ , ensuring proper rotations (note that

systematically incorporating improper rotations is also possible (Goemans and Williamson, 1995; Bandeira et al., 2013)). We estimate  $\theta_i$  by inverting (4), and register the signals by rotating signal  $i$  by  $-\theta_i$ . We note that, in our actual computations, the pairwise rotations  $\theta_{ij}$  are computed in a discrete setting, then the overall synchronization is performed in the continuum context to obtain  $\theta_i$ , and the results are rounded to give the closest discrete shift.

Importantly, this formulation also considers *higher-order* consistency information. For example, given our pairwise estimates  $R_{ij}$ , we know that relationships of the form

$$R(\theta_{ik})R(\theta_{kj}) \approx R(\theta_i)R(\theta_k)^T R(\theta_k)R(\theta_j)^T = R(\theta_i)R(\theta_j)^T \quad (9)$$

should also hold. Note that

$$(H^2)_{ij} = \sum_k R(\theta_{ik})R(\theta_{kj}); \quad (10)$$

therefore, *all* information of the form in (9) is contained in the matrix  $H^2$  (and higher order consistency information in its higher powers). Because  $H$  and  $H^2$  have the same eigenvectors, our problem formulation accounts for not only pairwise alignment information, but also these higher-order considerations.

### Diffusion maps (Coifman et al., 2005)

Given  $m$  data points  $x_1, \dots, x_m$  (typically vectors in a high-dimensional vector space), we want to find a coordinate transformation  $y(x)$  that preserves local geometry: points that are “close” in the original space should also be “close” in the coordinates  $y$ . The first step is to construct the matrix  $W \in \mathbb{R}^{m \times m}$ , where  $W_{ij}$  is large if points  $x_i$  and  $x_j$  are “close.” We use a diffusion kernel,

$$W_{ij} = \exp\left(-\frac{d^2(x_i, x_j)}{\epsilon^2}\right), \quad (11)$$

where  $d(x_i, x_j)$  is a pairwise distance between  $x_i$  and  $x_j$  (often the Euclidean distance), and  $\epsilon$  is a characteristic scale. Points less than  $\epsilon$  apart are thus considered “close” and points farther than  $\epsilon$  apart are considered “far away”.  $\epsilon$  can be chosen using several techniques (see, for example (Coifman et al., 2008; Rohrdanz et al., 2011)); here, we take  $\epsilon$  to be 1/4 of the median of the pairwise distances for the two-dimensional images, and 1/2 of the median of the pairwise distances for the three-dimensional z-stacks.

To find the coordinate  $y$ , we want solve the following optimization problem (Belkin and Niyogi, 2003)

$$\arg \min_y \sum_{ij} W_{ij} (y(x_i) - y(x_j))^2. \quad (12)$$

We first compute the diagonal matrix  $D$ , where  $D_{ii} = \sum_{j=1}^m W_{ij}$ , and the matrix  $A$ , where

$$A = D^{-1}W. \quad (13)$$

We calculate the eigenvectors  $\phi_1, \phi_2, \dots, \phi_m$ , ordered such that  $|\lambda_1| \geq |\lambda_2| \geq \dots \geq |\lambda_m|$ . Because the matrix  $A$  is similar to the symmetric matrix  $D^{-1/2}WD^{-1/2}$ ,  $A$  is guaranteed to have real eigenvalues and real, orthogonal eigenvectors. Because the matrix  $A$  is row-stochastic,  $\lambda_1 = 1$  and  $\phi_1$  is a constant vector; this is a trivial solution to (12). The next eigenvector,  $\phi_2$ , is the (non-trivial) solution to (12), so that  $\phi_2(j)$ , the  $j^{\text{th}}$  entry of  $\phi_2$ , gives the “new” coordinate for data point  $x_j$  (i.e.,  $\phi_2(j) = y(x_j)$ ). In our application, we have assumed that this *single* direction of variability, parameterized by  $\phi_2$ , is one-to-one with time. Ordering the data by  $\phi_2(j)$  will then, effectively, order them in time. The procedure generalizes when the data lie on higher-dimensional manifolds (not just curves) in data space, where leading eigenvectors can give subsequent embedding coordinates for the data.

### Vector diffusion maps (Singer and Wu, 2012)

In vector diffusion maps, given data points  $x_1, \dots, x_m$ , one first constructs the matrix  $S \in \mathbb{R}^{md \times md}$ , with the  $i, j^{\text{th}}$  block of  $S$ ,  $S_{ij}$ , defined as

$$S_{ij} = A_{ij}H_{ij} \quad (14)$$

where  $A_{ij} \in \mathbb{R}$  (defined in (13)) pertains to the diffusion kernel between data points, and  $H_{ij} \in \mathbb{R}^{d \times d}$  (defined in (5)) pertains to the pairwise alignment between data points. It is important to note that distance  $d(x_i, x_j)$  used in the diffusion kernel in (11) is the distance between data points *after* pairwise alignment, i.e., the minimum distance between all possible shifts of the two data points (which is obtained in (17)). In the language of symmetry groups, this distance is a metric between the orbits induced by the relevant symmetry group.

One then computes the eigenvalues  $\lambda_1, \lambda_2, \dots, \lambda_{md}$  and eigenvectors  $\phi_1, \phi_2, \dots, \phi_{md}$  of  $S$ , ordered such that  $|\lambda_1| \geq |\lambda_2| \geq \dots \geq |\lambda_{md}|$ . These eigenvectors contain information about *both* the optimal rotations (the “synchronization” component) and the variation of the data *after* the spatial symmetries have been factored out (in our case, their temporal variation). Assuming that the data (after symmetries have been factored out) are relatively closely clustered, it is reasonable to expect, as in angular synchronization, that the top (block) eigenvector of  $S$  contains approximations of the optimal rotations, which can be computed in the same way from (8). We then expect subsequent eigenvectors to contain information about the main direction(s) of data variability modulo the geometric symmetries.

In general, the embedding coordinates are given by

$$\psi_{k,l}(i) = \langle \phi_k(i), \phi_l(i) \rangle, \quad (15)$$

where  $\phi_k(i) \in \mathbb{R}^d$  denotes the  $i^{\text{th}}$  block of  $\phi_k$ . If we assume that the rotations and the dynamics are uncoupled and therefore separable, then the eigenvectors of  $S$  have the following structure: each block eigenvector contains estimates of the optimal rotations (up to a constant rotation)



multiplied by the corresponding embedding coordinate (a scalar). As the first diffusion maps coordinate is constant over the data, the first block eigenvector contains only the optimal rotations. The second block eigenvector (eigenvectors  $d + 1$  through  $2d$ ) contains the optimal rotations, each multiplied by their second diffusion maps coordinate. We can therefore recover this diffusion maps coordinate by taking inner products of the columns of the second block eigenvector with columns of the first block eigenvector. The  $j^{\text{th}}$  embedding coordinate will be given by  $\psi_{k,l}$ , where  $jd + 1 < k \leq (j + 1)d$  and  $1 \leq l \leq d$ , and we select  $k, l$  such that the coordinate  $\psi_{k,l}$  has the largest variability, i.e., the  $j^{\text{th}}$  coordinate is  $\psi_{k,l}$ , where  $k, l$  is the solution to

$$\max_{\substack{jd + 1 \leq k \leq (j + 1)d \\ 1 \leq l \leq d}} \sum_i \psi_{k,l}(i)^2. \quad (16)$$

## Registering images

To register sets of images, the first step is to compute the optimal alignments between pairs of images. Practically, we have square images discretized as pixels (rather than continuous functions on the plane). For each image pair  $I_i$  and  $I_j$  we compute

$$\theta_{ij} = \arg \min_{0^\circ \leq \theta < 360^\circ} \|g(I_j, \theta) - I_i\|^2. \quad (17)$$

where  $g(I_j, \theta)$  is image  $I_j$  rotated around the center of the square by  $\theta$  degrees. The norm,  $\|\cdot\|$ , is the Euclidean norm between the pixel intensities of the channels. The domain of the image (a square) is not invariant to our rotations; however, the pixels near the corners of the square are preprocessed to have zero intensity, and so the norm can be meaningfully computed as long as the main image does not “move out of” the original square. Image rotation is performed with the `imwarp` function in MATLAB, using linear interpolation to estimate the pixel intensities after rotation. The missing pixels in the corners of the rotated image are taken to have zero intensity. The solution to (17) is not easily computed, as the objective function will most likely be nonconvex. Therefore, instead of using an optimization procedure, we discretize the search space and exhaustively search to find the solution (for the results presented, we use  $10^\circ$  discretization steps). Although computationally demanding, this “embarrassingly parallelizable” direct enumeration approach is not prohibitive here. Once we have computed  $\theta_{ij}$  for all image pairs, we can proceed with the vector diffusion maps procedure. The rotation matrices returned from vector diffusion maps can be used to calculate the angle of rotation for each image (by inverting (4)), and the function  $g$  as described previously is then used to rotate the images.

## The eigenvalue spectrum

We can use the eigenvalues from (vector) diffusion maps to help deduce the dimensionality of the data. In diffusion maps, the largest eigenvalue will always be 1 and correspond to the trivial (constant) eigenvector, and  $|\lambda_k|$  gives a measure of the importance of coordinate  $\phi_k$ . We therefore expect to see a “spectral gap” in the eigenvalues which separates the meaningful coordinates from those corresponding to noise. However, some embedding coordinates which appear meaningful according to the eigenvalues may be harmonics of previous coordinates (Ferguson et al., 2010), and one must visually check for correlations among potential embedding coordinates before deducing the true dimensionality of the data.

In vector diffusion maps, the importance of each coordinate is measured by the product of the corresponding eigenvalues (i.e., the importance of  $\psi_{k,l}$  is given by  $|\lambda_k \lambda_l|$ ). We again expect to see a “spectral gap” in these eigenvalue products between those corresponding to meaningful coordinates (modulo higher harmonics) and those corresponding to noise.

## Smooth trajectories from registered and ordered images

Once we have registered and ordered the images, we can smooth the resulting trajectory to obtain a “stereotypic” developmental trajectory. Let  $I_1, \dots, I_m$  denote the set of *registered and ordered* images (so  $I_j$  is the  $j^{\text{th}}$  image in the ordered set). We define the average image at time  $\tau$ , denoted  $\bar{I}_\tau$  (where  $1 \leq \tau \leq m$ ), as a (Gaussian) weighted average of the images,

$$\bar{I}_\tau = \frac{\sum_j \exp\left(-\frac{|j-\tau|^2}{\sigma^2}\right) I_j}{\sum_j \exp\left(-\frac{|j-\tau|^2}{\sigma^2}\right)} \quad (18)$$

where  $\sigma$  is the scale of the Gaussian filter. For the images in Fig. 5 and 6, we take  $\sigma = 2$ . See (Kemelmacher-Shlizerman et al., 2011) for a more detailed discussion.

## References

- Ahuja, S., Kevrekidis, I. G. and Rowley, C. W. (2007). Template-based stabilization of relative equilibria in systems with continuous symmetry. *Journal of Nonlinear Science* **17**, 109–143.
- Bandeira, A. S., Singer, A. and Spielman, D. A. (2013). A Cheeger inequality for the graph connection Laplacian. *SIAM Journal on Matrix Analysis and Applications* **34**, 1611–1630.
- Belkin, M. and Niyogi, P. (2003). Laplacian eigenmaps for dimensionality reduction and data representation. *Neural Computation* **15**, 1373–1396.

**Canny, J.** (1986). A computational approach to edge detection. *IEEE Transactions on Pattern Analysis and Machine Intelligence* pp. 679–698.

**Coifman, R. R., Lafon, S., Lee, A. B., Maggioni, M., Nadler, B., Warner, F. and Zucker, S. W.** (2005). Geometric diffusions as a tool for harmonic analysis and structure definition of data: Diffusion maps. *Proc. Natl. Acad. Sci. U.S.A.* **102**, 7426–7431.

**Coifman, R. R., Shkolnisky, Y., Sigworth, F. J. and Singer, A.** (2008). Graph Laplacian tomography from unknown random projections. *IEEE Trans. Image Process.* **17**, 1891–1899.

**Ferguson, A. L., Panagiotopoulos, A. Z., Debenedetti, P. G. and Kevrekidis, I. G.** (2010). Systematic determination of order parameters for chain dynamics using diffusion maps. *Proc. Natl. Acad. Sci. U.S.A.* **107**, 13597–13602.

**Goemans, M. X. and Williamson, D. P.** (1995). Improved approximation algorithms for maximum cut and satisfiability problems using semidefinite programming. *Journal of the ACM (JACM)* **42**, 1115–1145.

**Kemelmacher-Shlizerman, I., Shechtman, E., Garg, R. and Seitz, S. M.** (2011). Exploring photobios. In *ACM Trans. Graph.*, volume 30, p. 61.

**Rohrdanz, M. A., Zheng, W., Maggioni, M. and Clementi, C.** (2011). Determination of reaction coordinates via locally scaled diffusion map. *J. Chem. Phys.* **134**, 124116.

**Shlens, J.** (2005). A tutorial on principal component analysis. *Systems Neurobiology Laboratory, University of California at San Diego*.

**Singer, A.** (2011). Angular synchronization by eigenvectors and semidefinite programming. *Appl. Comput. Harmon. Anal.* **30**, 20–36.

**Singer, A. and Wu, H.-T.** (2012). Vector diffusion maps and the connection Laplacian. *Commun. Pure Appl. Math.* **65**, 1067–1144.

### Outline of algorithm used to register and order images

1. Compute the alignments for each pair of images, as described in (17). Retain both the optimal pairwise rotations as well as the minimum distances obtained when pairs are optimally aligned.
2. Compute the corresponding rotation matrices  $R(\theta_{ij})$  from (4).
3. Select  $\epsilon$  for use in the diffusion maps kernel. Taking  $\epsilon$  to be 25 – 50% of the median of the pairwise distances often yields good results.
4. Compute the matrix  $S$  in (14).  $A_{ij}$  is computed from (11) and (13), using the pairwise distances from step 1, and  $H_{ij} = R(\theta_{ij})$  are computed in step 2.
5. Compute the eigenvalues  $\lambda_1, \lambda_2, \dots, \lambda_{2m}$  and eigenvectors  $\phi_1, \phi_2, \dots, \phi_{2m}$  of  $S$ , ordered such that  $|\lambda_1| \geq |\lambda_2| \geq \dots \geq |\lambda_{2m}|$ .
6. Estimate the optimal three-dimensional rotation for each image: stack the first two eigenvectors  $\phi_1, \phi_2$  into a  $2m \times 2$  matrix, and then divide this matrix into  $m$   $2 \times 2$  blocks,  $\hat{R}_1, \dots, \hat{R}_m$ . Compute the estimated rotations for each of these  $m$  blocks as in (8). If most of the rotations are improper ( $\det(R) = -1$ ), flip the sign of one of the eigenvectors.
7. Multiply each estimated rotation  $R_{i,est}$  by  $R_{1,est}^T$  (so that  $R_{1,est}$  will become the identity matrix).
8. For each image  $i$ , compute the optimal rotation to align the image by converting  $R_{i,est}^T$  (note the transpose) to the corresponding angle using (4).
9. Compute the first embedding coordinate  $\psi_{k,1}(i)$  as described in (15) and (16), where  $3 \leq k \leq 4$ .
10. To order the images, sort them by the values of this embedding coordinate  $\psi_{k,l}(i)$ .

| Data set                               | VDM Rank Correlation | PCA Rank Correlation |
|--|----------------------|----------------------|
| <i>Drosophila</i> gastrulation (live)  | 0.9989               | 0.8137               |
| Zebrafish epiboly                      | 0.9955               | 0.6351               |
| <i>Drosophila</i> gastrulation (fixed) | 0.9716               | 0.8658               |
| <i>Drosophila</i> wing discs           | 0.9436               | 0.9381               |

Table 1: Comparison between rank correlation coefficients when ordering using the first vector diffusion maps (VDM) embedding coordinate, and rank correlation coefficients when ordering by the first principal component analysis (PCA) (Shlens, 2005) projection coefficient. For ordering using PCA, we computed the first principal component of the registered images, and then ordered the images by the projection coefficients onto this first mode. The PCA ordering is always less accurate than the vector diffusion maps ordering. In the zebrafish data set, the ordering is much less accurate using PCA, as the dynamics of the morphing and spreading of the cell mass are highly nonlinear. The PCA and VDM orderings are comparable for the wing disc data; this is to be expected, as the tissue simply grows in time.



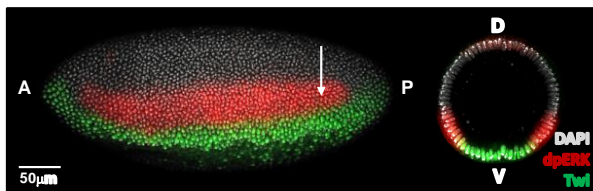


Fig. S1: (Left) A lateral view of a *Drosophila* embryo stained with DAPI (gray), dpERK (red), and Twi (green). The embryo is presented so that the anterior (A) side is to the left and the posterior (P) side is to the right. The arrow indicates the position where the cross-section of an embryo is imaged. (Right) A dorsoventral view of the cross-section of the *Drosophila* embryo. The dorsal (D) side is up and the ventral (V) side is down. Images were collected at the focal plane  $\sim 18\%$  from the posterior pole of an embryo (arrow in the left image).

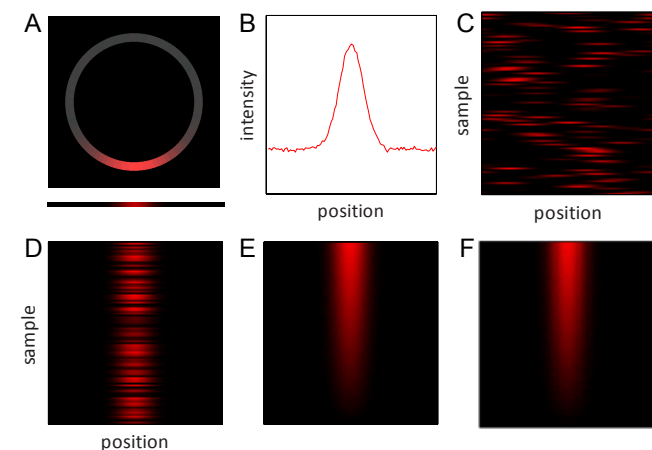
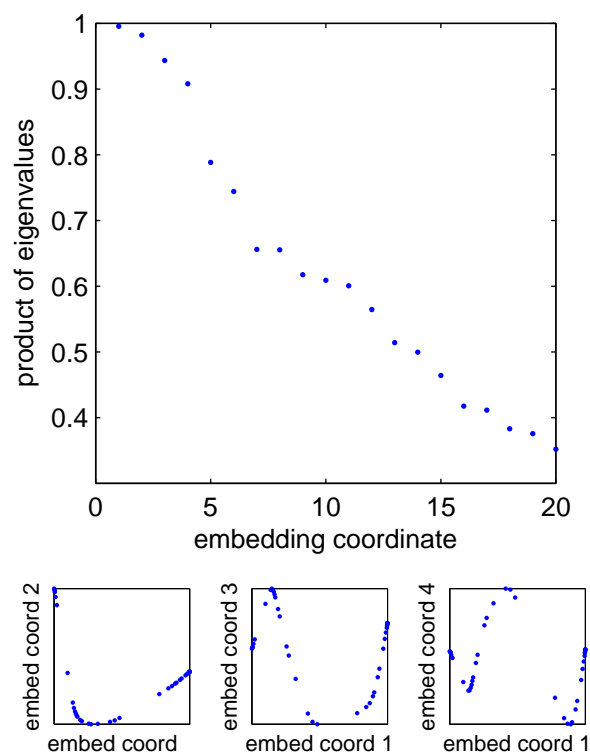


Fig. S2: Synthetic data set used to illustrate the data processing algorithms. (A) One-dimensional concentration profile on a ring (top), and the corresponding profile on a line (bottom). (B) Intensity corresponding to the profile in A. (C) An ensemble of concentration profiles, each of the form described in A. Each row in the array corresponds to a single profile. (D) The profiles in C, now registered using angular synchronization. (E) The profiles in D, now temporally ordered using diffusion maps. (F) The profiles in C, registered and temporally ordered in a single step using vector diffusion maps.

Fig. S3: Eigenvalue spectra for the *Drosophila* live imaging data set presented in Fig. 3. Note that there is a gap after the fourth eigenvalue product. Below are the second, third, and fourth embedding coordinate plotted versus the first embedding coordinate. Note that coordinates 2–4 are higher harmonics (and thus simple functions) of coordinate 1, and are therefore not informative about structure in the data set. We can conclude that the data set is effectively one-dimensional and can be parameterized/ordered by coordinate 1.

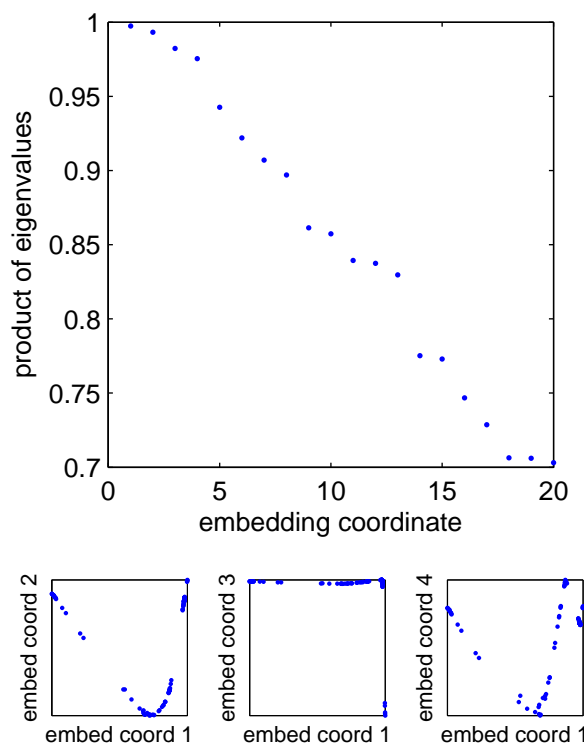


Fig. S4: Eigenvalue spectra for the zebrafish data set presented in Fig. 4. Note that there is a gap after the fourth eigenvalue product. Below are the second, third, and fourth embedding coordinate plotted versus the first embedding coordinate. Note that coordinates 2–4 are higher harmonics (and thus simple functions) of coordinate 1, and are therefore not informative about structure in the data set. It is not immediately obvious that coordinate 3 is a harmonic of coordinate 1; the distortion in the plot is due to density effects in the data (the developmental changes are slower towards the beginning of the trajectory, and so there is a higher density of images in this portion of the one-dimensional curve). We can conclude that the data set is effectively one-dimensional and can be parameterized/ordered by coordinate 1.

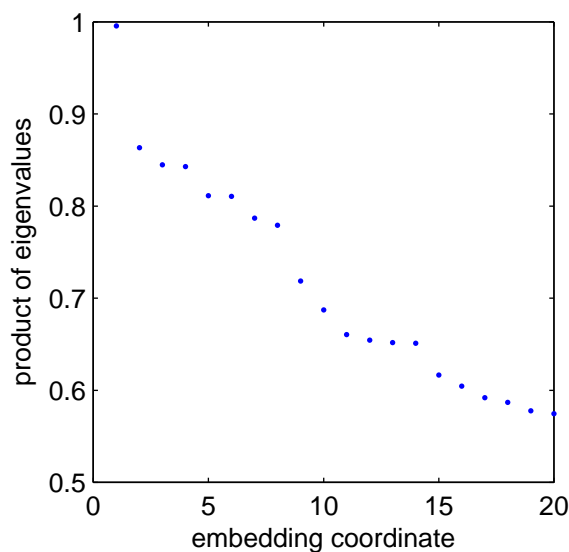


Fig. S5: Eigenvalue spectra for the fixed *Drosophila* images presented in Fig. 5. Note that there is a gap after the first eigenvalue product. We can conclude that the data set is effectively one-dimensional and can be parameterized/ordered by coordinate 1.

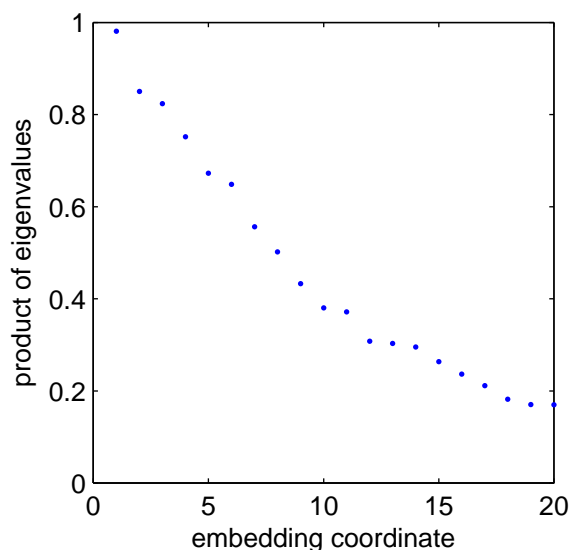


Fig. S6: Eigenvalue spectra for the wing disc data set presented in Fig. 6. Note that there is a gap after the first eigenvalue product. We can conclude that the data set is effectively one-dimensional and can be parameterized/ordered by coordinate 1.